# Anharmonic lattice dynamics and superionic transition in AgCrSe$_2$

Jingxuan Ding[a], Jennifer L. Niedziela[b], Dipanshu Bansal[c], Jiuling Wang[a], Xing He[a], Andrew F. May[d], Georg Ehlers[e], Douglas L. Abernathy[f], Ayman Said[g], Ahmet Alatas[g], Yang Ren[g], Gaurav Arya[a], and Olivier Delaire[a,h,i,1]

[a]Department of Mechanical Engineering and Materials Science, Duke University, Durham, NC 27708; [b]Nuclear Nonproliferation Division, Oak Ridge National Laboratory, Oak Ridge, TN 37831; [c]Department of Mechanical Engineering, Indian Institute of Technology Bombay, Mumbai, Maharashtra 400076, India; [d]Materials Science and Technology Division, Oak Ridge National Laboratory, Oak Ridge, TN 37831; [e]Neutron Technologies Division, Oak Ridge National Laboratory, Oak Ridge, TN 37831; [f]Neutron Scattering Division, Oak Ridge National Laboratory, Oak Ridge, TN 37831; [g]Advanced Photon Source, Argonne National Laboratory, Lemont, IL 60439; [h]Department of Physics, Duke University, Durham, NC 27708; [i]Department of Chemistry, Duke University, Durham, NC 27708

## 1 SI materials and Methods

**Material synthesis.** A polycrystalline sample of AgCrSe$_2$ was synthesized by reacting high-purity elemental starting materials in a sealed quartz ampoule. The starting materials were ground and pressed into a 1/2 inch diameter pellet. The pellet was heated slowly to 600 °C and annealed for 12 h, then the reaction was raised to 850 °C for 24 h. The sample purity was characterized using powder X-ray diffraction collected on a PANalytical X'Pert PRO diffractometer using monochromatic copper K$_{\alpha,1}$ radiation (1.5406 Å), and all diffraction peaks were indexed to the expected AgCrSe$_2$ phase. Single crystals of AgCrSe$_2$ were grown by annealing polycrystalline AgCrSe$_2$ and CrCl$_3$ in a quartz ampoule laying within a tube furnace at a set point temperature of 925 °C for 200 h.

**Inelastic neutron scattering.** INS measurements were performed on AgCrSe$_2$ powder (mass $\sim$ 4.7 g) using the time-of-flight Cold Neutron Chopper Spectrometer (CNCS) and on powder (mass $\sim$ 8.0 g) using the Wide Angular-Range Chopper Spectrometer (ARCS) at the Spallation Neutron Source at Oak Ridge National Laboratory (1, 2). The powder was sealed in a 3/8 inch diameter thin-walled aluminum can. Elastic line energy resolution was measured using a vanadium standard and verified using the sample at low temperature.

In the CNCS measurements, we mounted the Al can in a bottom-loading closed-cycle refrigerator with a sapphire switch thermal stage. An oscillating radial collimator (3) to limit the divergence of the diffracted beam and incident beam slits to reduce the total beam size were employed to minimize background scattering from sample environment. We used this setup to reach $T = 10, 40, 300, 460, 530, 600, 700$, and 750 K. Two incident energies, 4 and 12 meV, in a high-flux configuration were chosen to acquire a dataset fast with reasonable resolutions. Empty can measurements were performed with different incident slit size while the rest configurations remain unchanged. One measurement of the empty can background scattering was made at 300 K in the slit down configuration, and the rest were made with a wider beam size. The ratio of these two configurations was calculated to rescale the empty can data.

In the ARCS measurements, we used a top-loading closed-cycle refrigerator with a hot stage. Incident energy $E_i = 80$ meV was used to cover the whole phonon energy range and $E_i = 20$ meV renders finer resolution to capture the details of the low-energy phonon modes. Data were collected at 300, 450, 520, and 650 K and the reversibility of the phase transition was confirmed using data collected while cooling down from 650 K with $E_i = 80$ meV. The Fermi chopper frequencies were 300 and 420 Hz for 20 and 80 meV, respectively. The t-zero chopper frequency was 90 Hz. These configurations provided an estimated elastic line energy resolution of 0.7 meV at $E_i = 20$ meV, which decreases to 3.5 meV at $E_i = 80$ meV. An oscillating radial collimator was used, and the empty can background scattering data were collected with an identical configuration as sample measurement.

The collected data were transformed from instrument coordinates to the physical momentum transfer, $\mathbf{Q}$, and energy transfer, $E$, using algorithms implemented in Mantid analysis software (4), and the data were then normalized by the total incident neutron flux and the detector efficiency was corrected with a vanadium empty can measurement. Corrections corresponding to the ratio of the incident and the final wave vectors were also applied. For $S(E)$ cuts, datasets from $E_i = 4$ and 12 meV measured at CNCS were combined by matching intensities at $E = 2$ meV, integrating over $0.7 \le |\mathbf{Q}| \le 2.5 \, \text{Å}^{-1}$ and $1 \le |\mathbf{Q}| \le 4 \, \text{Å}^{-1}$, respectively. The $E_i = 12$ meV data illustrates the evolution of the 3.5 meV mode with temperature clearly, and the $E_i = 4$ meV data gives fine resolution close to the elastic line, which allows us to access the QENS signal. Curves for different temperatures were vertically offset. The analysis of the phonon density of state (DOS) was performed within the incoherent scattering approximation and corrections for multiphonon and multiscattering were applied (5). The elastic peak region ($E < 2$ meV) was removed, and the region was extrapolated using a Debye-like quadratic energy dependence to get the (neutron-weighted, NW) DOS:

$$g_{NW}(E) = \sum_i f_i \frac{\sigma_i}{m_i} g_i(E)$$

$$g_i(E) = \sum_{j,\mathbf{q}} |e_i(j,\mathbf{q})|^2 \delta(E - E(j,\mathbf{q})), \qquad [1]$$

where $f_i$, $\sigma_i$, $m_i$ and $g_i(E)$, $e_i(j, \mathbf{q})$, $E(j, \mathbf{q})$ are the atomic fraction, neutron total cross section, atomic mass, partial density of states, phonon eigenvectors and phonon energies of atom $i$. The neutron scattering cross sections of Ag, Cr, and Se are 4.99, 3.49, and 8.3 barns, respectively. As a result, we can weight the simulated DOS similarly and directly compare with the experimental DOS. We normalized all phonon DOS by the area of total phonon DOS in this study. In our simulations, we applied experimental resolution of $E_i = 20$ and $80\,\text{meV}$ to the low and high energy portions, and neutron weighted the contributions from different atoms and stitched datasets at the same energy as experiments. Note, we are still applying the quadratic dispersion relation in Debye model close to zero energy for all phonon DOS and normalizing by the area under the curves. Ideally, the lower energy portion should be replaced by $\frac{S(E) \times E}{n(E)+1}$ (6), especially at high temperature, to show the transfer of spectrum weight from vibration (phonon DOS) to stochastic diffusion (QENS), provided that the elastic line is being subtracted properly.

**X-ray scattering.** Diffraction pattern measurements were performed on AgCrSe$_2$ powder $\sim 0.1\,\text{g}$ with hard X-rays ($E_i = 105.708\,\text{keV}$) at Sector 11-ID-C of Advanced Photon Source, Argonne National Laboratory (7). The powders were mounted and heated in a thin copper disk (1 mm) with an inner radius of 1 mm, clamped in a Linkam TS1500 stage in nitrogen atmosphere. The heating and cooling ramp rates were $10\,\text{K/min}$. and data were collected continuously as temperature increased. In XRD, to track the intensity as a function of temperature, we subtract linear backgrounds from these Bragg peak intensities and fit them with Gaussian functions. The results are shown in main text in Fig. 1$B$ inset and Fig. S2 inset. All three peaks follow a power-law decay in intensity and become constant above the transition temperature. These Bragg peak intensities clearly illustrate a transition behavior with the transition temperature around nominal temperatures 500 K. The higher value than the reported 475 K should due to the temperature gradient between the heating component and the sample in experiments.

IXS measurements were performed on AgCrSe$_2$ single crystals, mounted on standard copper post with high temperature silver paste (PELCO-16047), using the high-resolution IXS beamline HERIX (8, 9) at Sector 30 of Advanced Photon Source, Argonne National Laboratory. The samples were approximately $50\,\mu\text{m}$ thick to maximize the signal and were measured in the transmission configuration. An X-ray single crystal diffractometer was used to check the crystal quality and later on confirmed by a transmission camera during alignment process at the spectrometer. The measured crystals were of high quality with single domains. Sample mosaics were about 0.1 degree in all directions. The incident energy was $23.7\,\text{keV}$ ($0.5226\,\text{Å}$) and the energy resolution measured with a plastic standard was $1.3\,\text{meV}$. The measured resolution was used to fit the spectra and extract phonon linewidths.

The IXS intensity is proportional to the single-crystal coherent dynamical structure factor:

$$S(\mathbf{Q}, \omega) = \left| \sum_d f_d(\mathbf{Q}) \exp(-W_d)[\mathbf{Q} \cdot \mathbf{e}_d(\mathbf{q}, j)] M_d^{-1/2} \exp(i\mathbf{Q} \cdot \mathbf{r}_d) \right|^2 \frac{<n> + 1/2 \pm 1/2}{\omega_{\mathbf{q},j}} \delta(\omega \pm \omega_{\mathbf{q},j}), \qquad [2]$$

where $d$ is the atom index (and $\mathbf{r}_d$ the atom position) in the conventional cell, $f_d(\mathbf{Q})$ is the x-ray form factor for atom $d$. $\mathbf{q}, \omega_s$ ($E_s = \hbar\omega_s$) are the phonon wave vector and eigenvalue corresponding to the branch index $j$, $W_d$ is the Debye–Waller factor and $\mathbf{Q}$ is the wave vector transfer. The phonon dispersions, $E = \hbar\omega(\mathbf{q})$, were extracted by fitting peak positions in measured spectra using a DHO profile convoluted with the HERIX energy resolution:

$$S(E) = R * I(E)$$
$$I(E) = A \frac{\{\frac{1}{2} \pm \frac{1}{2} + n(|E|)\} \times 2E\Gamma_{LW}}{(E^2 - E_0^2)^2 + (2E\Gamma_{LW})^2} + B, \qquad [3]$$

where $S(E)$, $R$ and $B$ are the observed scattering intensity, instrument energy resolution and constant background. $n(E)$ is the Bose-Einstein distribution function at phonon energy transfer $E$, $E_0$ is the renormalized phonon energy in the presence of damping. $A$ and $\Gamma_{LW}$ are the amplitude and phonon half width at half maximum.

Three temperatures 80, 300, and $560\,\text{K}$, which were controlled by a beryllium shielded closed-cycle refrigerator, were used to track the phonon evolutions through the superionic transition. Sample orientation was defined with (104) and (110) Bragg peaks. Phonon polarizations and energies were tracked along $[1-2\text{H}, 1+\text{H}, \xi]$, $[1, 0, \text{L}]$ and $[-2+\text{H}, 1, 0]$ directions, where H, L and $\xi$ indicates the direction of phonon propagation. Each point was count between 30 to 90 seconds. At $\mathbf{Q} = 0.9$, 1.05, 0 ($\boldsymbol{\tau} = 1, 1, 0$, $\mathbf{q} = -0.1, 0.05, 0$), we observe weak longitudinal acoustic (LA) phonon, contributing a shoulder to the primary TA phonon peak (Fig. S10). Nevertheless, we could connect the behavior of TA phonons with their wave vector $\mathbf{q}$ from the observations mentioned above: at small $\mathbf{q}$, where the TA branches are more dispersive, TA phonons persist at all measured temperatures; at large $\mathbf{q}$, where the TA branches are non-dispersive, TA phonons smear out in the superionic phase.

**Density Functional Theory Calculations.** Density Functional Theory (DFT) based on first-principles was used as the calculation method as implemented in the Vienna ab initio Simulation Package (VASP 5.3) (10–12) where the exchange-correlation function takes the generalized gradient approximation (GGA) in the Perdew–Burke–Ernzerhof (PBE) form (13, 14). A electronic

Olivier Delaire.
E-mail: olivier.delaire@duke.edu

$k$-point mesh of $13 \times 13 \times 3$ centers at $\Gamma$ was used in structure relaxation of $AgCrSe_2$ pseudo-hexagonal conventional cell (12 atoms). The plane-wave energy cut-off of $500\,eV$ and the electronic self-consistent loop convergence of $10^{-8}\,eV$ were used. The atomic positions were optimized until the residual forces on all atoms were smaller than $0.1\,meV\cdot\mathring{A}^{-1}$. We used projector-augmented-wave potentials, which explicitly included 12 valence electrons for Cr $(2p^6 3d^5 4s^1)$, 11 for Ag $(4d^{10} 5s^1)$, and 6 for Se $(2s^2 2p^4)$. The relaxed lattice constants are $a = b = 3.758\,\mathring{A}$, $c = 21.057\,\mathring{A}$, 2% larger in $a$ and 0.4% smaller in $c$ than experiments reported previously $a = b = 3.663\,\mathring{A}$ and $c = 21.154\,\mathring{A}$ (15). Phonon dispersions and phonon DOS were calculated using the harmonic approximation applying finite displacement approach as implemented in Phonopy (16). A $4 \times 4 \times 1$ supercell of the conventional cell (192 atoms) was used. The atomic displacement amplitude was $0.01\,\mathring{A}$ in all cases. A k-point mesh of $2 \times 2 \times 2$ was used considering the supercell size.

The spin polarization (SP) effects are included in the DFT calculations with a magnetic momentums of about $3\,\mu_B$ on each Cr atom. The SP calculations stabilize the structure and yield a semiconducting electronic band structure. We include this effect because magnetism is important in $AgCrSe_2$, and it has being extensively investigated (17). We note that non-spin polarized calculations result in lattice parameters with 10% difference than experiments. Unphysical metallic electronic band structure and unstable phonons are observed throughout the Brillouin zone. The lattice tends to melt in NSP AIMD calculations even at $300\,K$. A strong antiferromagnetic correlation is expected, as in experiment, the magnetic dispersion remain up to $200\,K$. Adding LDA+U (18) or Van der Waals interaction to the non-spin polarized calculation provide similar wrong predictions.

**Ab initio calculations.** Ab initio molecular dynamics simulations were performed on the same $4 \times 4 \times 1$ supercell as phonon calculations. A $\Gamma$-point mesh with a plane-wave cut-off energy of $700\,eV$ was used to fit the effective energy surface in the Temperature Dependent Effective Potential (TDEP) (19, 20) method. The electronic self-consistent loop convergence was set to $10^{-5}\,eV$. AIMD simulations were performed using NVE-ensemble with Nosé–Hoover thermostat. Two temperatures, 300 and $600\,K$, were chosen to represent the ordered and disordered phase. The simulation trajectories were at least $13\,ps$ long with a time step of $2\,fs$. The remaining AIMD parameters were identical to $0\,K$ DFT simulations. The lattice constants were constrained to be the same as $0\,K$ during the simulation, nevertheless, the simulations with two temperatures clearly showed different behavior across the order–disorder transition. Power spectra at specific $\mathbf{Q}$ were obtained by projecting the AIMD trajectories onto the corresponding harmonic phonon eigenvectors and applying FFT directly to get the intensity as a function of phonon frequency as implemented in Dynaphopy (21). For pair distribution functions, we only considered bonds lengths small than $7.5\,\mathring{A}$ because of the limited simulation box size. For the TDEP method, the accuracy of the effective potential is affected by the delocalization of Ag atoms between $\alpha$ and $\beta$ sites (occasional hops occur in $300\,K$ AIMD and become common in $600\,K$ AIMD) because TDEP tries to sample the energy surface by tracking atom pairs, but Ag hopping reorganizes nearest-neighbor distributions.

**Diffusion pathway and potential barrier.** We define a reaction pathway and obtain the free energy landscape from the trajectories of Ag ions when they hop from $\alpha$ sites to $\beta$ sites at $600\,K$. First, all the trajectories of Ag ions are mapped to one pair of adjacent $\alpha$ and $\beta$ sites. Then, the trajectories are projected onto a plane perpendicular to the shared edge, which makes the $\alpha$ and $\beta$ sites clearly distinguishable. We can obtain the probability density of Ag ions on this plane, as shown in main text Fig. 5D. Most Ag ions stay in $\alpha$– and $\beta$–tetrahedrons, and only a few Ag ions stay in the transition area. Next, we define a reaction coordinate $\theta$, which is the angle between the Ag ion and the center of the $\alpha$–tetrahedron, and the probability density of Ag ions along the reaction pathway, $P(\theta)$, can be obtained. Assuming that the probability distribution follows Boltzmann distribution, we can obtain the free energy landscape of Ag ions along the reaction pathway via

$$\Delta F = -k_B T \cdot \ln\left(\frac{P(\theta)}{P(\theta = 0)}\right), \tag{4}$$

where $k_B$ and $T$ are the Boltzmann constant and the temperature. The landscape yields an energy barrier of about $0.11\,eV$.

We also analyzed the time distribution for Ag ions to escape from the $\alpha$-tetrahedron (Fig. S15A) and $\beta$–tetrahedron (Fig. S15B) at $600\,K$. For an activation process, the distribution function of the escape time follows:

$$p(t) = \frac{1}{\tau_{ave}} \cdot \exp\left(-\frac{t}{\tau_{ave}}\right), \tag{5}$$

where $\tau_{ave}$ is the average escape time. We calculate the average time for Ag ions to escape from the $\alpha$-tetrahedron and $\beta$-tetrahedron sites, and then use Equ. 5 to predict the escape time distributions, which agree well with the time distributions from AIMD simulations.

1. Ehlers G, Podlesnyak AA, Niedziela JL, Iverson EB, Sokol PE (2011) The new Cold Neutron Chopper Spectrometer at the Spallation Neutron Source: Design and performance. *Review of Scientific Instruments* 82(8):085108.
2. Abernathy DL, et al. (2012) Design and operation of the wide angular-range chopper spectrometer ARCS at the Spallation Neutron Source. *Review of Scientific Instruments* 83(1):015114.
3. Stone MB, Niedziela JL, Loguillo MJ, Overbay MA, Abernathy DL (2014) A radial collimator for a time-of-flight neutron spectrometer. *Review of Scientific Instruments* 85(8):085101.
4. Arnold O, et al. (2014) Mantid—Data analysis and visualization package for neutron scattering and $\mu$SR experiments. *Nuclear Instruments and Methods in Physics Research Section A: Accelerators, Spectrometers, Detectors and Associated Equipment* 764:156–166.
5. Lin Y, Islam F, Kresh M (2018) Multiphonon: Phonon density of states tools for inelastic neutron scattering powder data. *Journal of Open Source Software* 3(21).
6. Squires GL (2009) *Introduction to the Theory of Thermal Neutron Scattering.* (Cambridge University Press, Cambridge), 3rd edition, p. 55.
7. Ren Y (2012) High-energy synchrotron x-ray diffraction and its application to in situ structural phase-transition studies in complex sample environments. *JOM* 64(1):140–149.
8. Toellner TS, Alatas A, Said AH (2011) Six-reflection meV-monochromator for synchrotron radiation. *Journal of Synchrotron Radiation* 18(4):605–611.
9. Said AH, Sinn H, Divan R (2011) New developments in fabrication of high-energy-resolution analyzers for inelastic X-ray spectroscopy. *Journal of Synchrotron Radiation* 18(3):492–496.
10. Kresse G, Hafner J (1993) Ab initio molecular dynamics for liquid metals. *Physical Review B* 47(1):558–561.
11. Kresse G, Furthmüller J (1996) Efficient iterative schemes for ab initio total-energy calculations using a plane-wave basis set. *Physical Review B* 54(16):11169–11186.
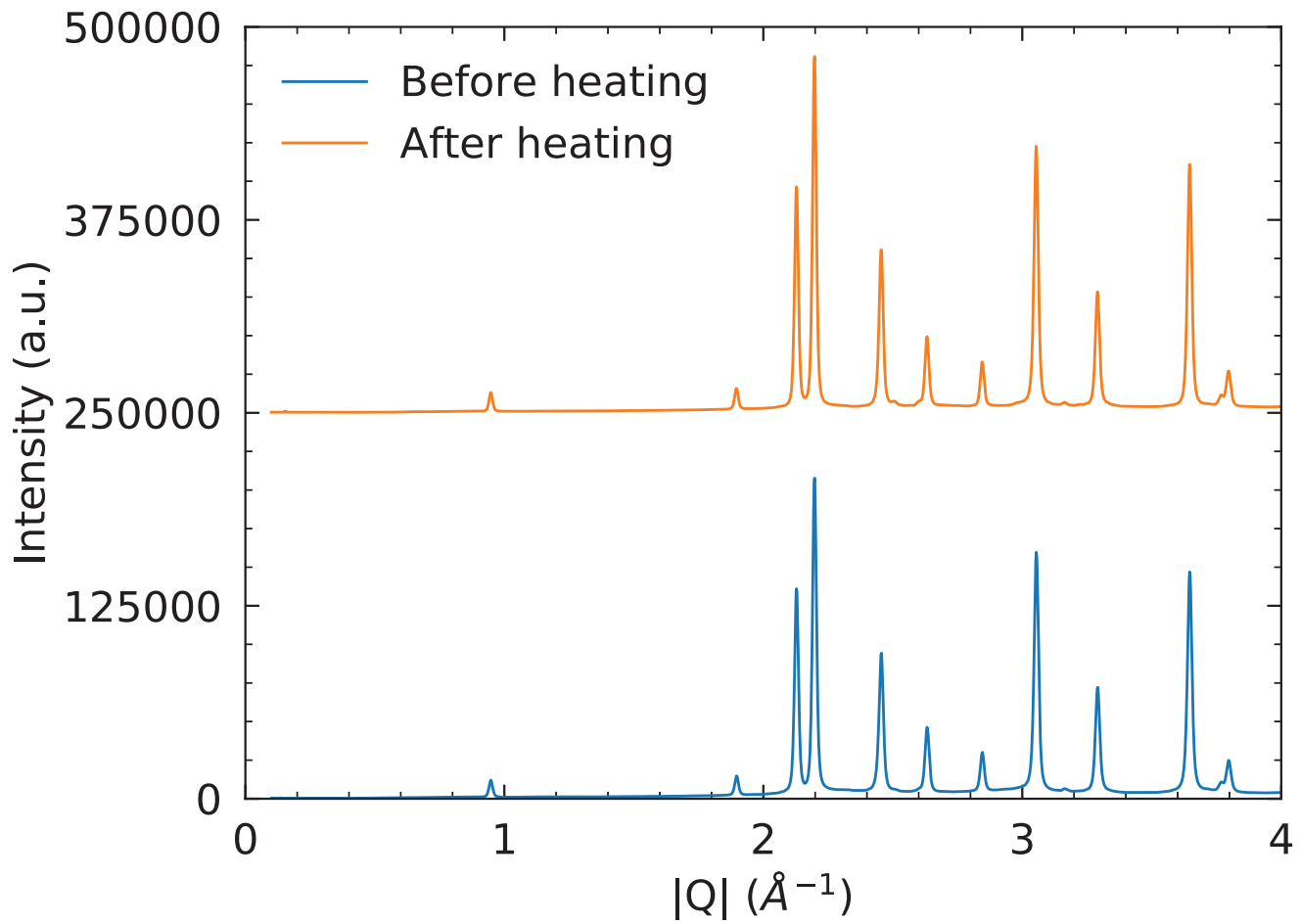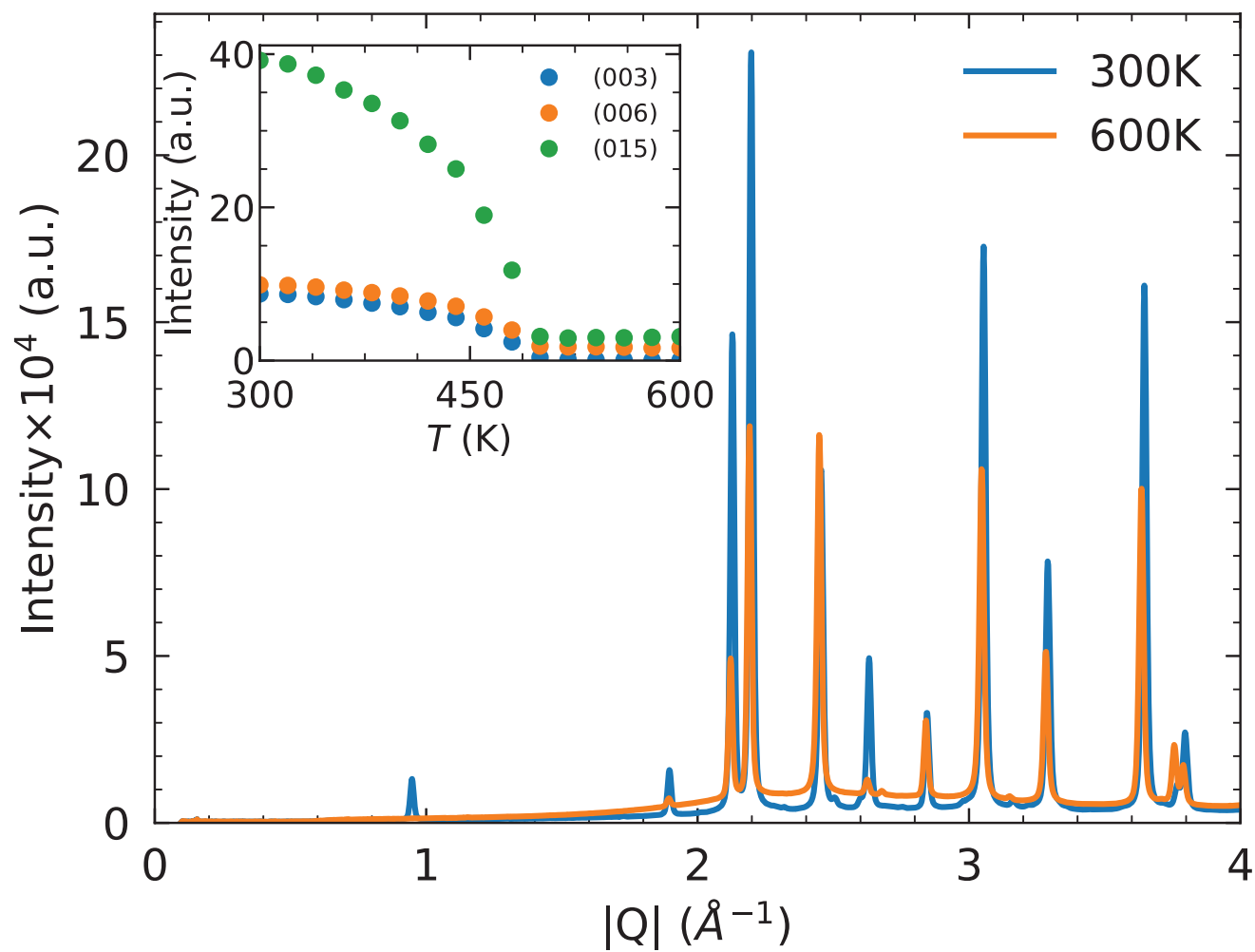
**Fig. S1.** (color) Reversibility check of XRD pattern at 300 K before and after heating. The diffraction patterns are identical, indicating that the superionic transition is reversible.

**Fig. S2.** (color) X-ray powder diffraction pattern at 300 (blue) and 600 K (orange) on cooling. Inset, the integrated intensities of (003), (006), and (015) Bragg peaks as a function of temperature, plotted as blue, orange, and green dots, respectively. The structural transition happens around nominal temperature 500 K.

Ding *et al.*

PNAS | **January 24, 2020** | vol. XXX | no. XX | **5**
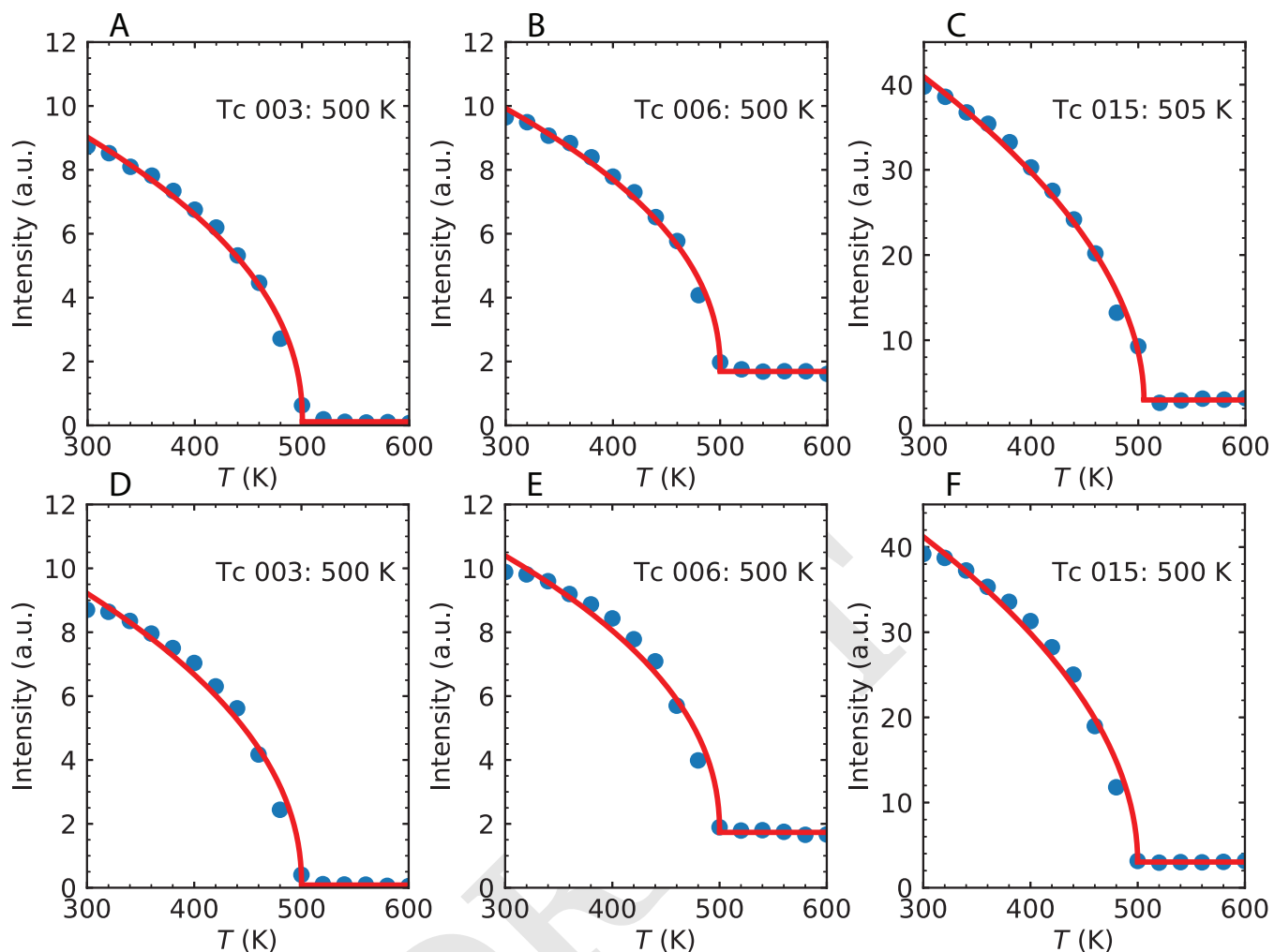
**Fig. S3.** (color) Power law fits of (003), (006), and (015) Bragg peak intensities from XRD on heating ($A$-$C$) and cooling ($D$-$F$).
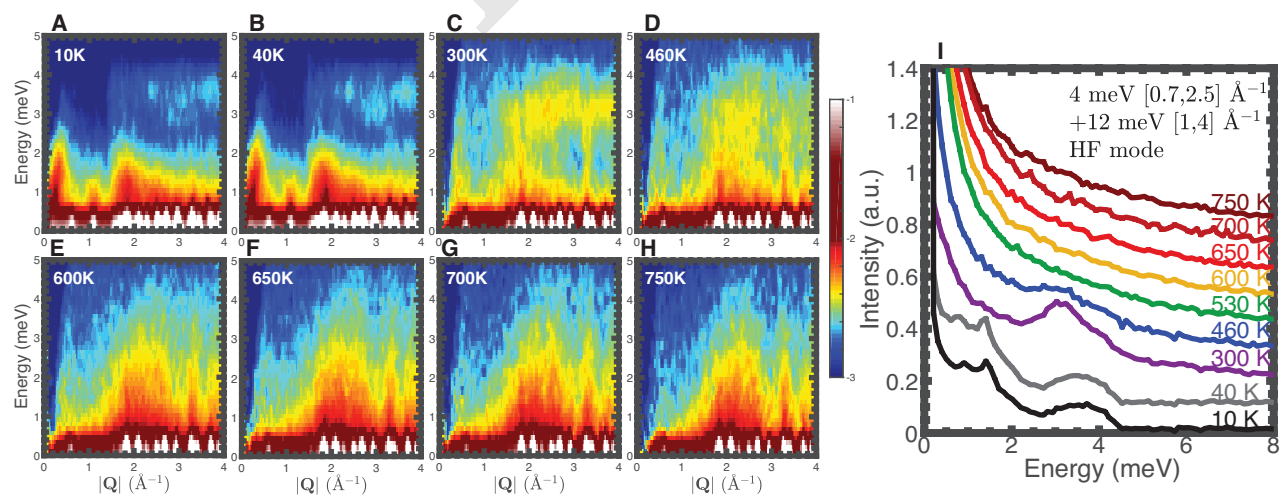


**Fig. S4.** (color) INS measurements reveal two behaviors in different portion of the acoustic phonon branch. $S(|\mathbf{Q}|, E)$ maps measured with $E_i = 12$ meV on CNCS at 10 K ($A$), 40 K ($B$), 300 K ($C$), 460 K ($D$), 530 K ($E$), 600 K ($F$), 700 K ($G$), and 750 K ($H$), respectively. ($I$) $S(E)$ cuts measured at CNCS. The $E_i = 4$ and 12 meV data are integrated over the range of $0.7 \leq |\mathbf{Q}| \leq 2.5 \, \text{Å}^{-1}$ and $1 \leq |\mathbf{Q}| \leq 4 \, \text{Å}^{-1}$, respectively. Spin wave exist below 300 K but magnetic quasi-elastic persist even at 300 K.

Ding *et al.*
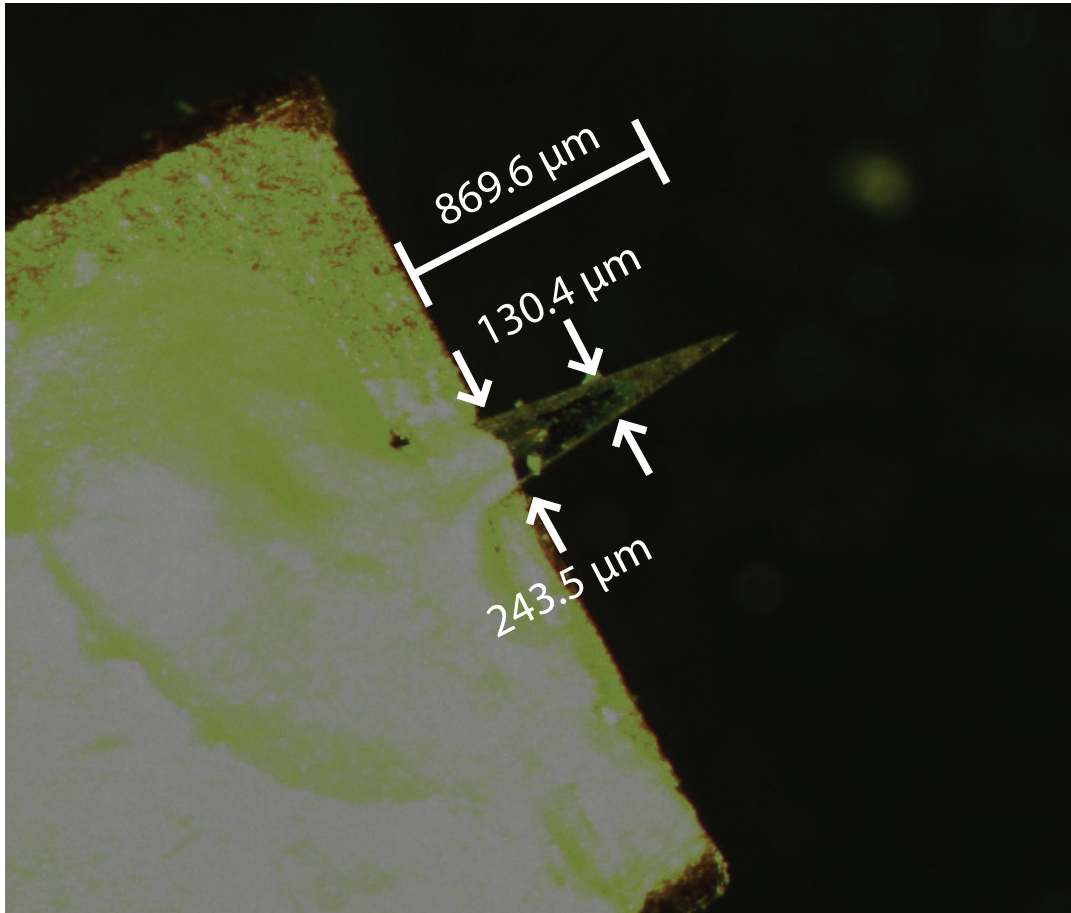
**Fig. S5.** (color) Optical microscope image of the IXS single crystal mounted on a copper post with high-temperature silver paste. The lengths are measured using reference grids in the microscope.
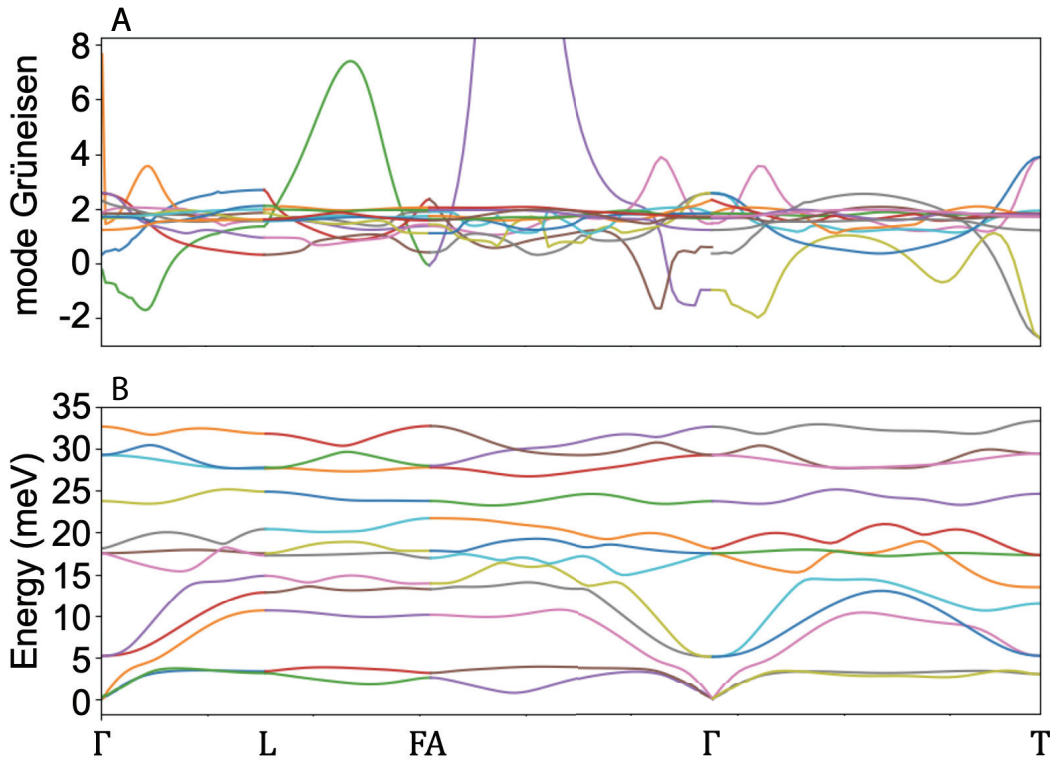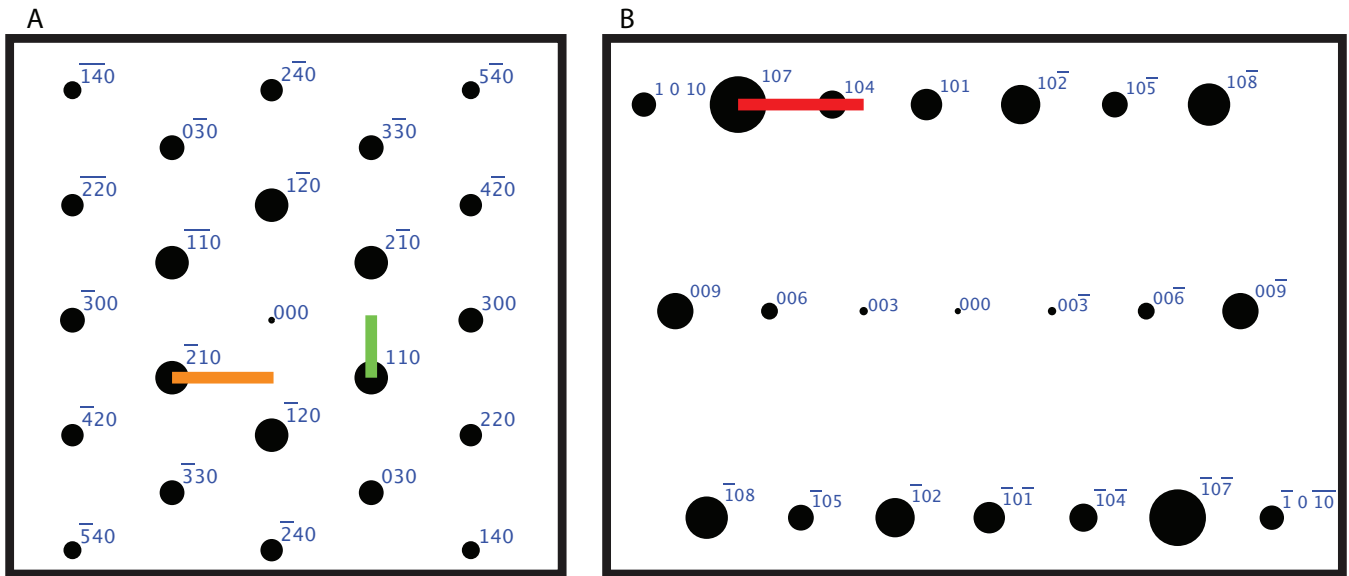
**Fig. S6.** (color) $(A)$ Mode Grüneisen parameters and $(B)$ phonon dispersion of AgCrSe$_2$. The phonons and the corresponding mode Grüneisen parameters are shown as the same color. High symmetry points are L = (0, 0.5, 0), FA = (0, 0.5, -0.5), T = (0.5, 0.5, -0.5) with respect to primitive axis. The negative mode Grüneisen parameter originate from TA modes near zone center, which explained the stiffening seen in IXS data. The large values between L and FA (7) or FA and $\Gamma$ (57) belong to the lowest TA. The mode Grüneisen parameters of this TA branch is volume sensitive. We applied an isothermal expansion/contraction of 0.5% in this calculation for simplicity.
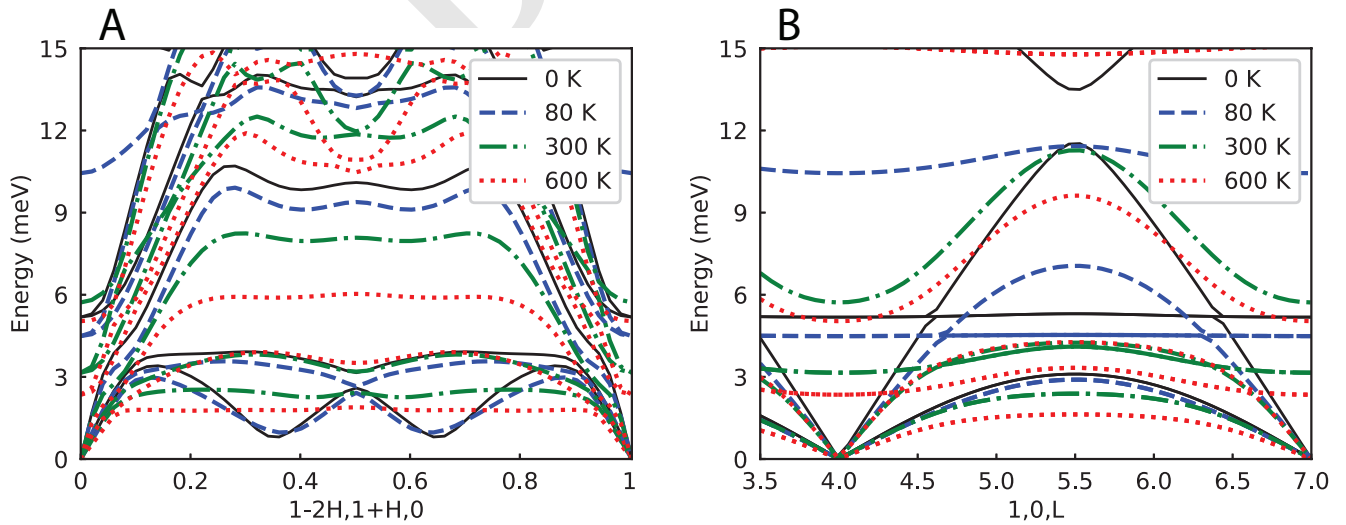


**Fig. S7.** (color) Renormalized phonon dispersions along $(A)$ $[1-2H, 1+H, 0]$ and $(B)$ $[1, 0, L]$ directions using TDEP methods. The phonon frequencies are strongly anharmonically renormalized as temperature increases.

Ding *et al.*

A

$\overline{1}40$  $\overline{2}40$  $\overline{5}40$

$0\overline{3}0$  $\overline{3}\overline{3}0$

$\overline{2}\overline{2}0$  $1\overline{2}0$  $\overline{4}\overline{2}0$

$\overline{1}\overline{1}0$  $2\overline{1}0$

$\overline{3}00$  .000  $\overline{3}00$

$\overline{2}10$  $110$

$\overline{4}20$  $\overline{1}20$  $220$

$\overline{3}30$  $0\overline{3}0$

$\overline{5}40$  $\overline{2}40$  $140$

B

1 0 10   107   104   101   10$\overline{2}$   10$\overline{5}$   10$\overline{8}$

009   006   003   000   00$\overline{3}$   00$\overline{6}$   00$\overline{9}$

$\overline{1}08$   $\overline{1}05$   $\overline{1}02$   $\overline{1}0\overline{1}$   $\overline{1}0\overline{4}$   $\overline{1}0\overline{7}$   $\overline{1}$ 0 $\overline{10}$

**Fig. S8.** (color) The reciprocal map of AgCrSe$_2$ projected onto the HK0 (left) and H0L (right) lattice planes. The measured directions for IXS are indicated by the orange, green, and red solid lines.

149   12.  Kresse G, Furthmüller J (1996) Efficiency of ab initio total energy calculations for metals and semiconductors using a plane-wave basis set. *Computational Materials Science* 6(1):15–50.
150   13.  Perdew J, Zunger A (1981) Self-interaction correction to density-functional approximations for many-electron systems. *Physical Review B* 23:5048–5079.
151   14.  Perdew J, Burke K, Ernzerhof M (1996) Generalized gradient approximation made simple. *Physical Review Letters* 77:3865–3868.
152   15.  Li B, et al. (2018) Liquid-like thermal conduction in intercalated layered crystalline solids. *Nature Materials* 17:226–230.
153   16.  Togo A, Oba F, Tanaka I (2008) First-principles calculations of the ferroelastic transition between rutile-type and CaCl$_2$-type SiO$_2$ at high pressures. *Physical Review B* 78(13).
154   17.  Damay F, et al. (2016) Localised Ag$^+$ vibrations at the origin of ultralow thermal conductivity in layered thermoelectric AgCrSe$_2$. *Scientific Reports* 6:23415.
155   18.  Anisimov VI, Zaanen J, Andersen OK (1991) Band theory and mott insulators: Hubbard U instead of stoner I. *Physical Review B* 44(3):943.
156   19.  Hellman O, Abrikosov IA, Simak SI (2011) Lattice dynamics of anharmonic solids from first principles. *Physical Review B* 84:180301(R).
157   20.  Hellman O, Abrikosov IA (2013) Temperature-dependent effective third-order interatomic force constants from first principles. *Physical Review B* 88:144301.
158   21.  Carreras A, Togo A, Tanaka I (2017) Dynaphopy: A code for extracting phonon quasiparticles from molecular dynamics simulations. *Computer Physics Communications* 221:221–234.
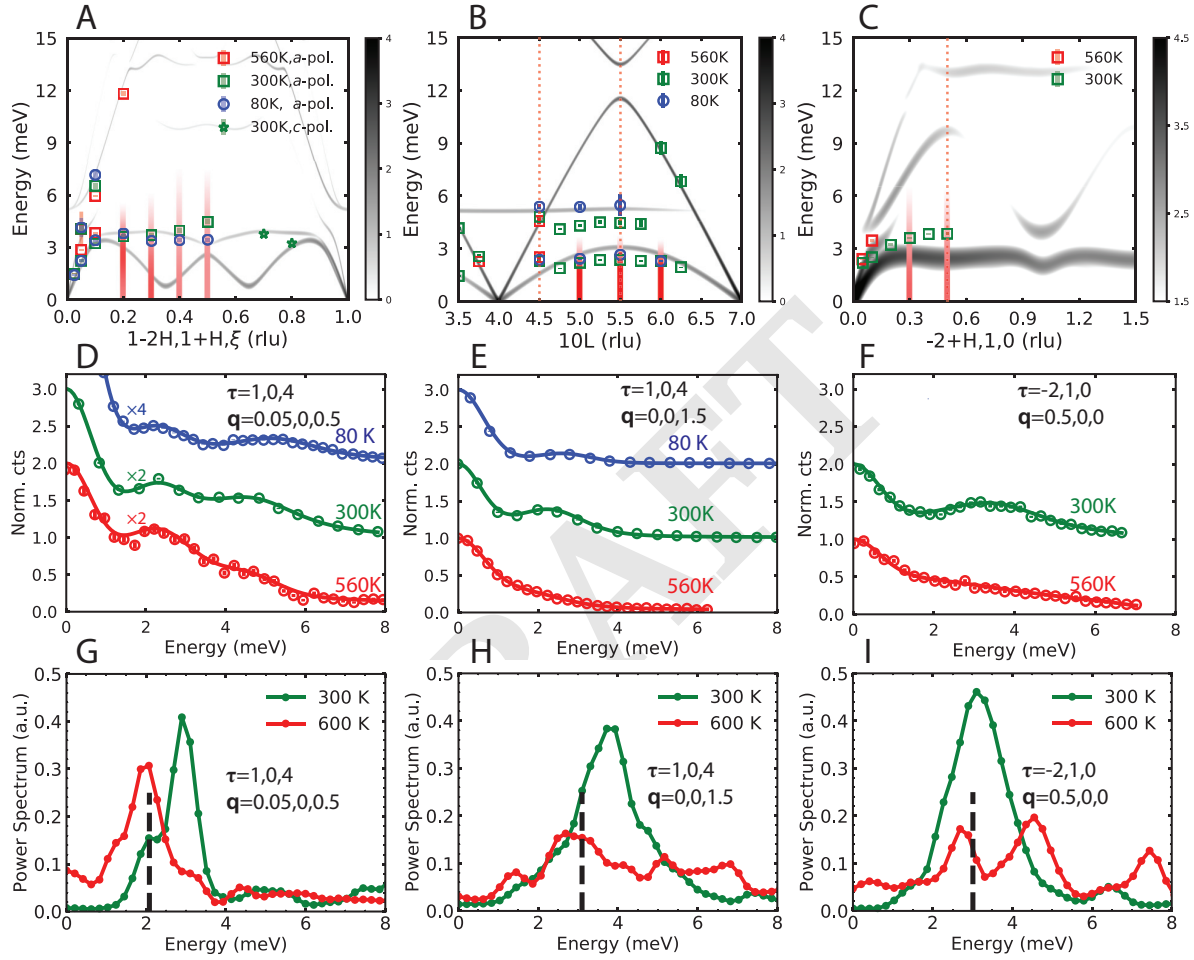
**Fig. S9.** (color) IXS measurements show selective breakdown of transverse acoustic phonon. ($A$–$C$) Momentum-resolved IXS measurements on single crystals of AgCrSe$_2$ with transverse polarization compared with DFT simulations of $S(\mathbf{Q},E)$. Phonon dispersions extracted along high symmetry directions are overlaid on DFT simulations. Abscissa labels indicate the momentum and space direction, and red vertical dashed lines indicate the locations of constant-$\mathbf{Q}$ spectra in panels. Red vertical bars are plotted to show the overdamped phonon at 560 K using fitted DHO. The intensities are shown in gradient color. In panel ($A$), $\xi = 0$ for $a$-polarized modes and $\xi = 15$ or 18 for $c$-polarized modes. ($D$-$F$) IXS spectra at specific $\mathbf{Q}$ across the superionic transition. The experimental data are shown as markers, and the solid lines are the corresponding fits using a DHO profile. All data are normalized by the maximum intensities, and the data at 80 and 300 K are vertically offset. ($G$–$I$) The power spectrum calculated from AIMD at specific $\mathbf{Q}$ for 300 and 600 K. Black dashed lines indicate the energies from harmonic approximation.
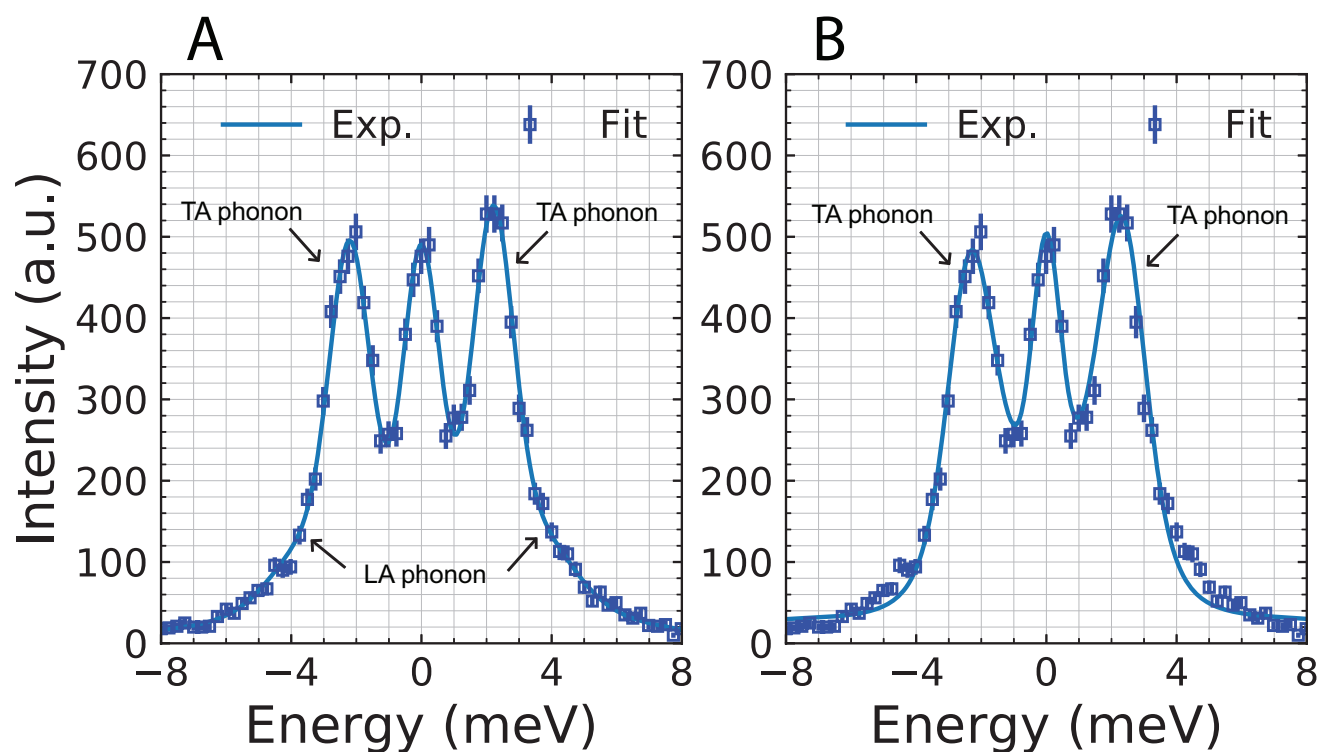
**Fig. S10.** (color) Fitting of **Q** = 0.9, 1.05, 0 with ($A$) two DHOs or ($B$) one DHO at 300 K. At this **Q**, phonons with transverse character dominate. The LA phonon appears only as a weak shoulder of the primary TA phonon. But if we do not consider LA phonon, the fitting deviates from the experiment.
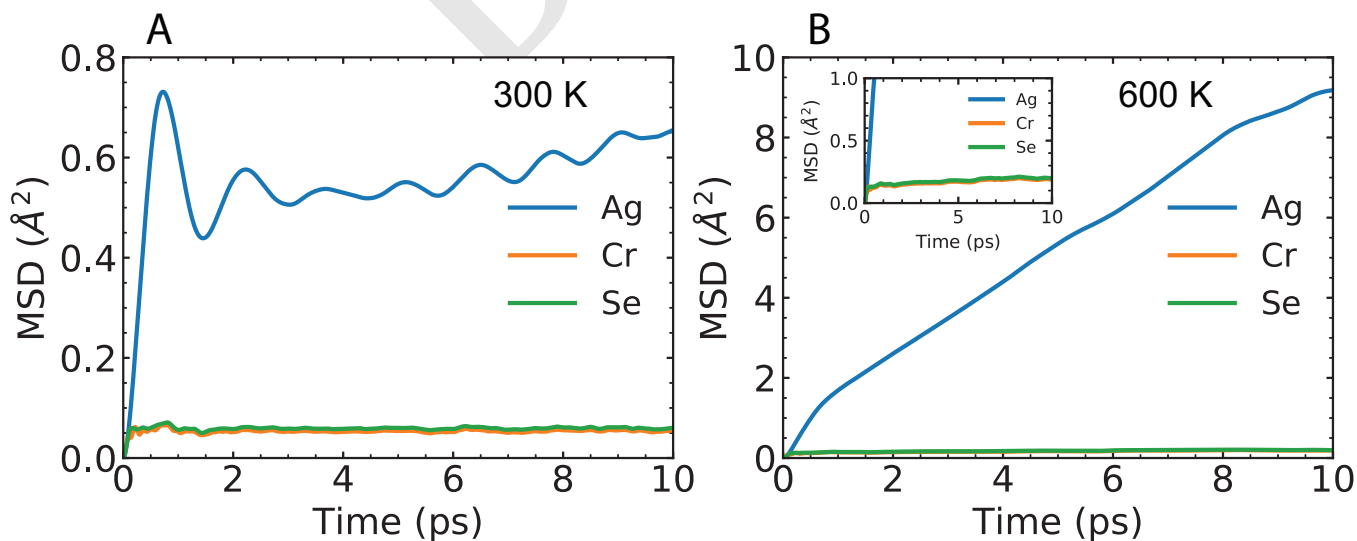


**Fig. S11.** (color) Decomposed mean square displacements of AgCrSe$_2$ for ($A$) 300 K and ($B$) 600 K. Silver, chromium, and selenium atoms are shown blue, orange and green, respectively. At 300 K, the vibration amplitudes of Ag atoms are larger than Cr and Se atoms. Cr and Se atoms vibrate with similar amplitudes. At 600 K, the vibration amplitudes of Cr and Se atoms increases (see [$B$] inset), but the MSD for Ag grows monotonically, reflecting the superionic diffusion.
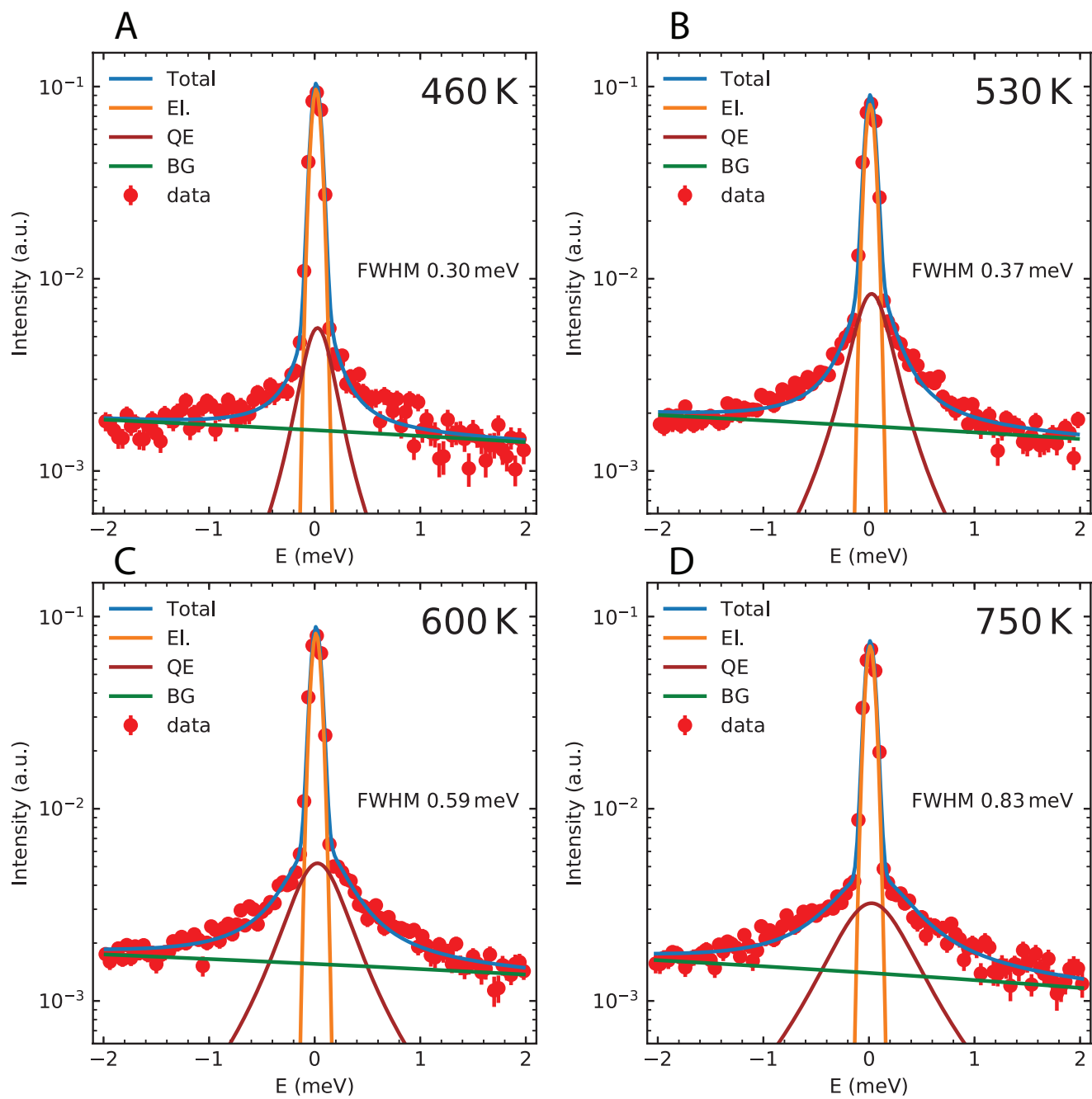
**Fig. S12.** (color) Decomposition of QENS fitting at $(A)$ 460 K, $(B)$ 530 K, $(C)$ 600 K, and 750 K. The width of QE part increase with temperature, indicating a faster diffusion of Ag atoms. Powder sample is measured at CNCS using $E_i = 4$ meV with elastic line energy resolution of 112 $\mu$eV FWHM.
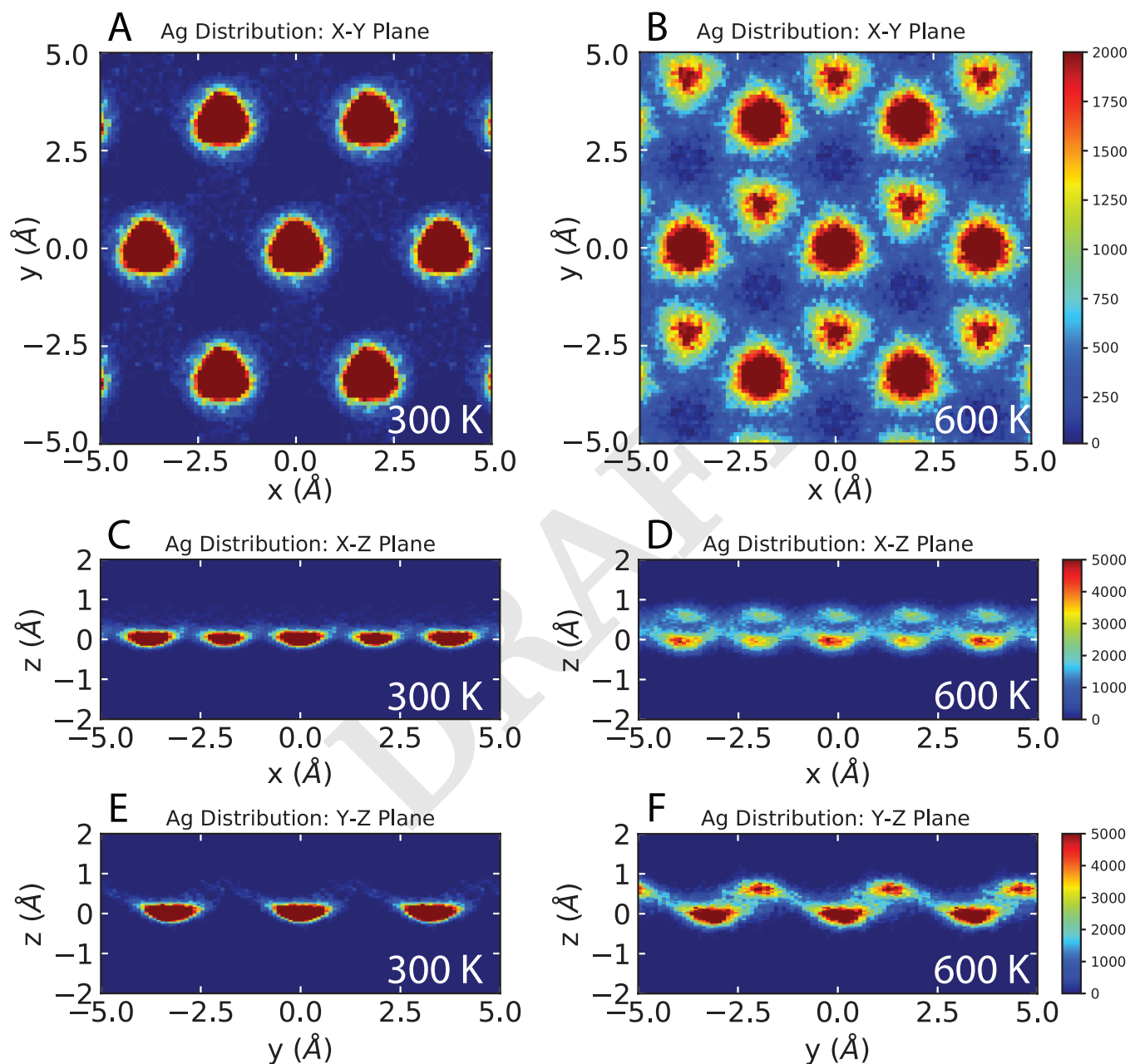
**Fig. S13.** (color) Probability distribution of Ag atoms from AIMD simulations projected on x–y, x–z, y–z plane at 300 and 600 K, respectively. At 300 K, Ag atoms are weakly bonded with other atoms. Therefore, Ag atoms tend to have large vibration amplitude, and the distribution of Ag atoms are anisotropic. At 600 K, Ag atoms hop between $\alpha$ and $\beta$ sites. Periodicity and three-fold symmetry are applied to achieve a better statistic.
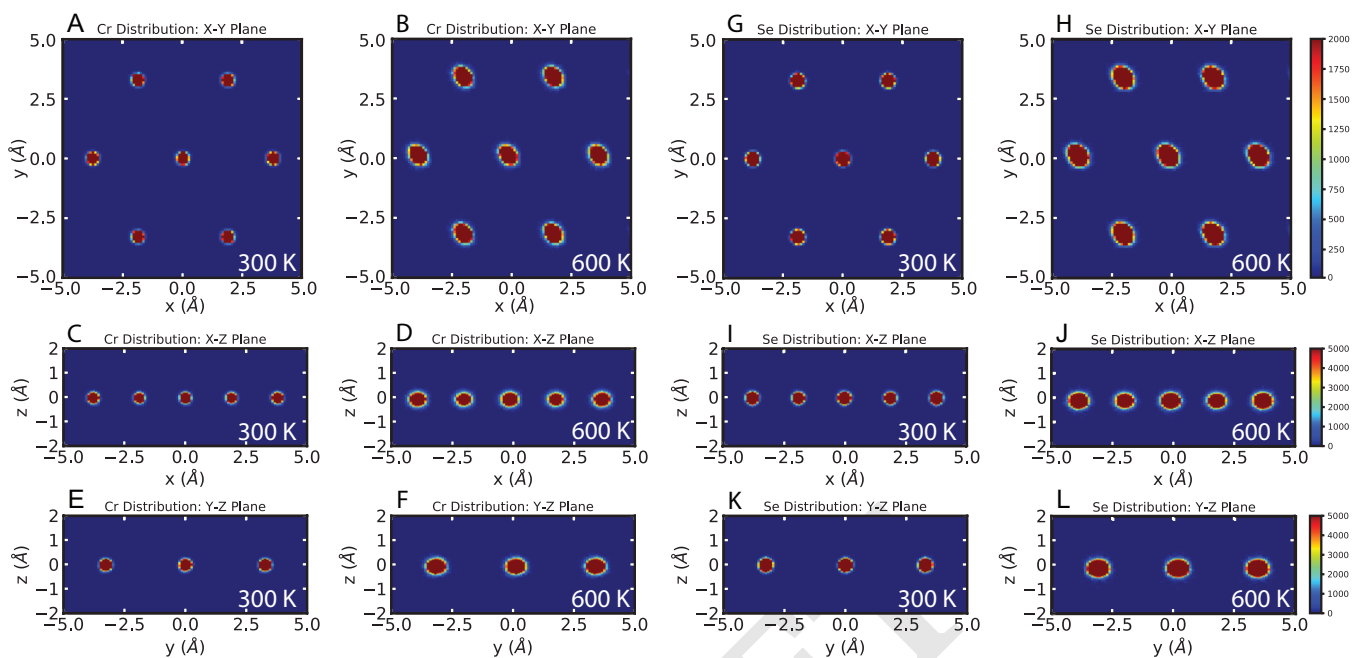
**Fig. S14.** (color) Probability distribution of ($A$–$F$) Cr and ($G$–$L$) Se atoms from AIMD simulations projected on x–y, x–z, y–z plane at 300 and 600 K, respectively. The vibration amplitudes are larger at 600 K than 300 K. The CrSe sublattices remain mostly unchanged across the superionic transition. Periodicity is applied.
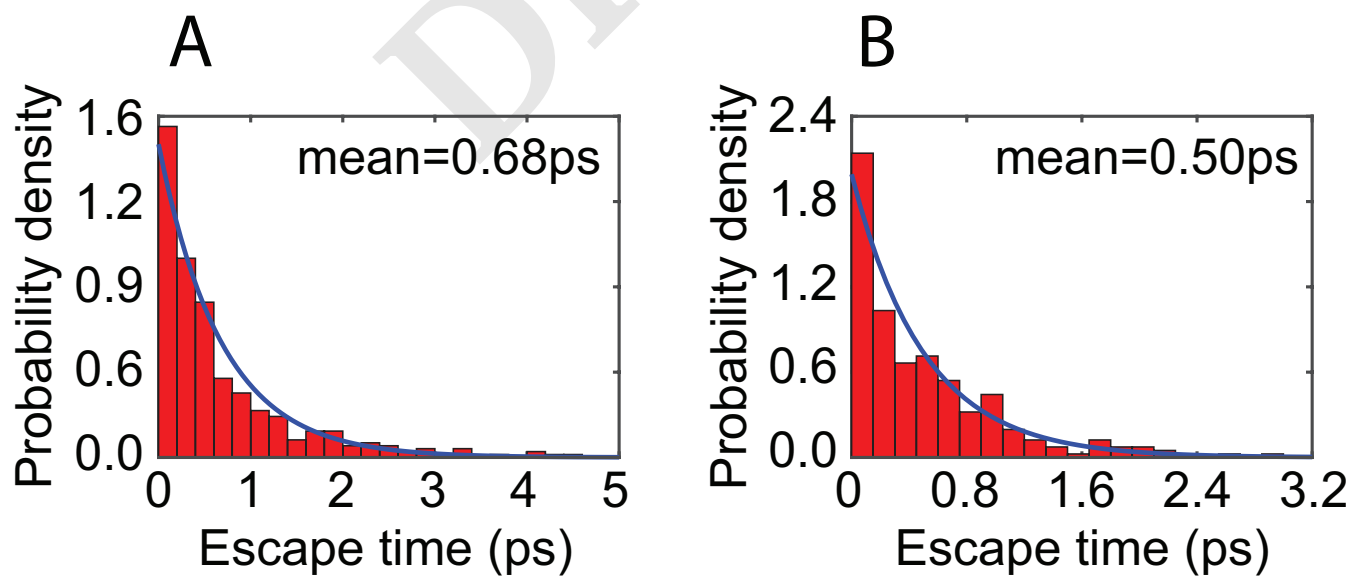


**Fig. S15.** (color) The time distribution for Ag ions to escape from the ($A$) $\alpha$-tetrahedron and ($B$) $\beta$-tetrahedron at 600 K from AIMD simulations. In our simulation, we observed 364 escape events ($A$) and 271 escape events ($B$).
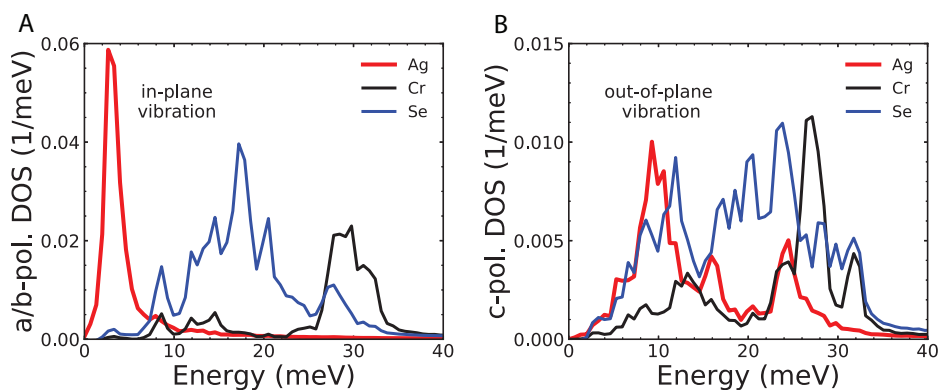
**Fig. S16.** (color) Site-projected phonon density of states at 300K ($A$) in-plane polarization ($B$) out-of-plane polatization.
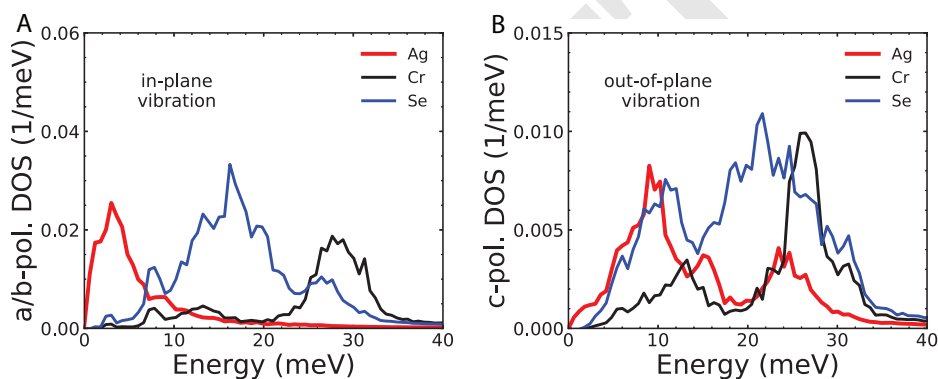


**Fig. S17.** (color) Site-projected phonon density of states at 600K ($A$) in-plane polarization ($B$) out-of-plane polatization.
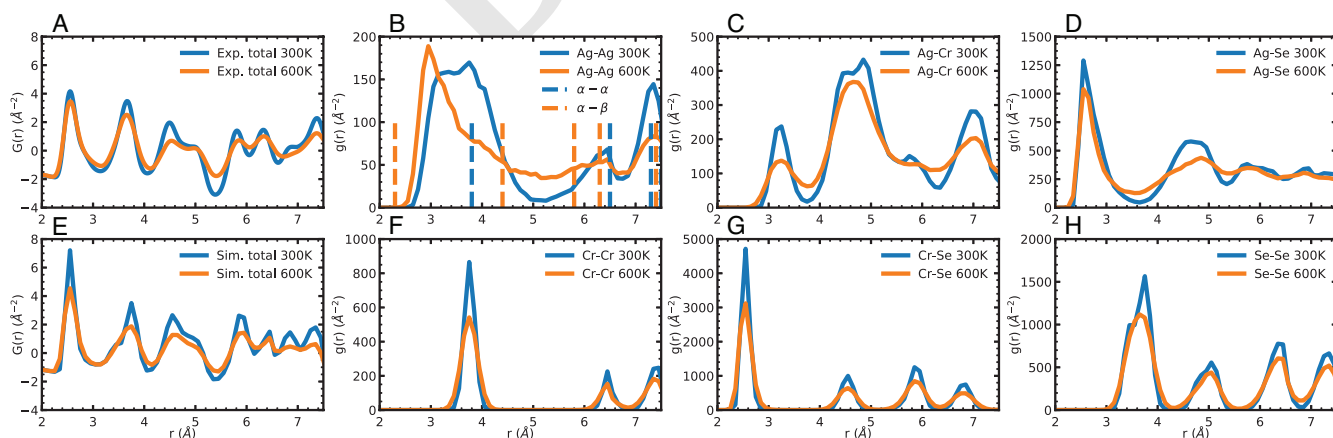


**Fig. S18.** (color) Pair distribution functions of AgCrSe$_2$. Reduced total pair distribution function from experiment ($A$) and simulation ($E$). Pair distribution function projected on each type of bond. ($B$) Ag–Ag bond, ($C$) Ag–Cr bond ($D$) Ag–Se bond, ($F$) Cr–Cr bond, ($G$) Cr–Se bond, ($H$) Se–Se bond. As the PDF of Ag-related bonds greatly broaden while Ag atoms exhibit diffusion behavior, the bond distributions form by Cr and Se remain mostly unchanged with small broadening, indicating a rigid crystalline behavior. Strong repulsion between Ag atoms are observed, as no Ag–Ag bond with length of 2.3 Å (the nearest $\alpha-\beta$ distance from crystal structure) appears in AIMD.